



## PAPER

## Performance investigation of LabPET II detector technology in an MRI-like environment

Narjes Moghadam<sup>1,4</sup>, Louis Arpin<sup>2</sup>, Romain Espagnet<sup>1</sup>, Jonathan Bouchard<sup>1</sup>, Nicolas Viscogliosi<sup>1</sup>, Roger Lecomte<sup>3</sup> and Réjean Fontaine<sup>1</sup><sup>1</sup> Groupe de Recherche en Appareillage Médical de Sherbrooke (GRAMS), Department of Electrical and Computer Engineering, Interdisciplinary Institute for Technological Innovation (3IT), Université de Sherbrooke, Sherbrooke, Québec, Canada<sup>2</sup> Imaging, Research and Technology (IR&T), Sherbrooke, Québec, Canada<sup>3</sup> Department of Nuclear Medicine and Radiobiology, Sherbrooke Molecular Imaging Center (CIMS), Université de Sherbrooke, Sherbrooke, Québec, Canada<sup>4</sup> Author to whom any correspondence should be addressed.E-mail: [Narjes.Moghadam@USherbrooke.ca](mailto:Narjes.Moghadam@USherbrooke.ca)**Keywords:** simultaneous PET/MRI, electromagnetic interference, composite shielding, eddy currentSupplementary material for this article is available [online](#)RECEIVED  
16 July 2019REVISED  
9 October 2019ACCEPTED FOR PUBLICATION  
14 November 2019PUBLISHED  
24 January 2020**Abstract**

The EMI-compatibility of the LabPET II detection module (DM) to develop a high-resolution simultaneous PET/MRI system is investigated. The experimental set-up evaluates the performance of two LabPET II DMs in close proximity to RF coils excited at three different frequencies mimicking the electromagnetic environments of 3 T, 7 T, and 9.4 T MRI scanners. A gradient coil, with switching frequency from 10 kHz to 100 kHz, also surrounds one of the DMs to investigate the effects of the gradient field on the individual detector performance, such as the baseline of the DC-voltage and noise level along with both the energy and coincidence time resolutions. Measurements demonstrate a position shift of the energy photopeaks ( $\leq 9\%$ ) and a slight deterioration of the energy and coincidence time resolutions in the presence of electromagnetic interferences from the gradient and RF coils. The electromagnetic interferences cause an average degradation of up to  $\sim 50\%$  of the energy resolution (in time-over-threshold spectra) and up to 18% of the timing resolution. Based on these results, a modified version of the DM, including a composite shielding as well as an improved heat pipe-based cooling mechanism, capable of stabilizing the temperature of the DM at  $\sim 40^\circ\text{C}$ , is proposed and investigated. This shielded version shows no evidence of performance degradation inside an MRI-like environment. The experimental results demonstrate that a properly shielded version of the LabPET II DM is a viable candidate for an MR-compatible PET scanner.

**1. Introduction**

Positron emission tomography (PET) is a powerful, non-invasive medical imaging modality having the ability to visualize and quantify the metabolic activity of tissues (Townsend 2008, Cherry *et al* 2018). However, because of the limited spatial resolution and the frequent lack of anatomical landmarks in PET images, there are several advantages in combining PET with a higher-resolution imaging modality, such as computed tomography (CT) or magnetic resonance imaging (MRI). Such dual-modality scanners provide better lesion localization, improve quantitative measurement accuracy (Kinahan *et al* 1998) and allow the correction of partial-volume effects (Soret *et al* 2007). Hybrid PET/CT, supported by image co-registration and fusion software, quickly became the clinical imaging standard at the turn of the millennium (Beyer *et al* 2000) despite its limitation related to organ motion, especially for heart and lung imaging (Levin *et al* 1988, Slomka 2004). On the other hand, even with the extra complexity, the combination of PET with MRI is gaining popularity owing to its higher soft-tissue contrast, the absence of ionizing radiation and the potential ability to acquire data perfectly co-registered in space and time (Townsend 2008). True simultaneous PET/MRI opens up new opportunities for studying dynamic processes with a high spatial and temporal resolution, for instance by providing kinetic information on the delivery of radioactive probes through the microcirculation while measuring its uptake by target tissues (Pichler *et al* 2008).

Nowadays, progress in solid-state photodetectors such as avalanche photodiodes (APDs) and silicon photomultipliers (SiPMs) made it possible to develop PET detectors working inside the high magnetic field of MRI scanners (Pichler *et al* 1997, Saoudi and Lecomte 1999). In addition, simultaneous PET and MRI imaging demonstrated diagnostic improvements in clinical MRI scanners (Grazioso *et al* 2006, Olcott *et al* 2015, Düppenbecker *et al* 2016) as well as in preclinical MRI scanners (Catana *et al* 2006, Schulz *et al* 2009, Kang *et al* 2015, Ko *et al* 2016, Schug *et al* 2016, Omidvari *et al* 2018). These works also pointed out that the key challenges for designing a simultaneous PET/MRI are the inhomogeneity of the main magnetic field owing to metallic and ferromagnetic materials, the electromagnetic interferences (EMI) and the temperature stabilization. In a PET/MRI scanner, there are two sources of EMI, namely low-frequency interferences, produced by gradient switching, and high-frequency RF interferences that may occur between the clock signal of the PET electronics and the RF signals of the MRI.

An inevitable source of interferences between PET and MRI is the magnetic field inhomogeneity resulting from the presence of components inserted in the MRI having different material susceptibility in comparison with air. In fact, ferromagnetic materials exert severe effects on the homogeneity (Schenck 1996) and the principal strategy to minimize such an impact consists of removing any ferromagnetic materials from the MRI field-of-view (FOV) or replacing them with low-susceptibility and low-conductivity metallic materials, as already investigated for the LabPET II detection module (DM) in Moghadam *et al* (2019). Furthermore, differential signaling eliminates the stray magnetic field effects and better preserves the homogeneity of the main magnetic field. Based on Larmor's equation, any variation in the magnetic field locally shifts the signal frequency and causes signal loss, signal pile-up or distortion artifacts.

The other source of electromagnetic interferences in an integrated PET/MRI originates from the fast switching gradients. Although the amplitude of the gradient field is smaller than the main magnetic field, the fast switching magnetic fields induce eddy currents in any closed electric and conductive path, as predicted by Faraday's law (Delso and Ziegler 2014). The eddy currents alter the electronics performance and generate heat that may affect the APD or SiPM gain and shift the breakdown voltage (Spanoudaki *et al* 2008), consequently modifying the number of prompt counts measured by detectors. Besides, based on Lenz's law, the currents induced on the metallic surfaces generate magnetic fields in the opposite direction of the primary source that alter the gradient field and cause MR image artifacts. To reduce the eddy current induction and its distortions on MR images, conductive structures, especially closed loops in electronic circuits, must be minimized in the MRI FOV. An additional reported effect of the fast switching gradient field is the distortion of the energy resolution owing to the instability of bias voltage in low-dropout (LDO) regulators and the deterioration of the timing resolution as a result of the deviation in the timestamp of individual events (Düppenbecker *et al* 2016).

The electromagnetic coupling between the RF coil and the PET distributed clock signal is the third source of electromagnetic interferences in a dual-modality PET/MRI scanner. The RF signals, detected in an MRI, are very weak; therefore, achieving a suitable signal-to-noise ratio (SNR) requires special attention. PET electronics circuits generate RF emissions that directly deteriorate the MRI SNR (Gebhardt *et al* 2014). Conversely, RF transmission within the same frequency range as the dynamic range of the analog band pass of the front end of PET electronics interferes with the PET data acquisition, unless careful consideration is given to EMIs while designing the printed circuit boards. Unlike copper shielding that mitigates PET electromagnetic signals at the price of generating undesired gradient interferences (Kang *et al* 2009, Pichler *et al* 2010), composite shielding layers, with lower conductivity than conventional metal shielding, such as carbon fiber or conductive polymer composites, have demonstrated their superior characteristics in this respect (Fox *et al* 2008, Düppenbecker *et al* 2012). Another approach consists of designing state-of-the-art printed circuit electronic boards with low electromagnetic susceptibility and compliance.

Although the LabPET II DM was demonstrated to work in both PET and CT modes (Bergeron *et al* 2015, Seydou Traore *et al* 2015), its performance in combination with an MRI still requires a further comprehensive investigation. The LabPET II DM was developed to achieve submillimeter spatial resolution and its modularity enables building application-specific devices for PET imaging from mice to human brains. The performance of the APD-based LabPET II DM is expected to be unaffected by strong magnetic fields. Its high-density front-end integrated electronics, supplying fully digitized data as an output, should make it less vulnerable to electromagnetic interferences. These characteristics represent prerequisites of MRI compatibility requirements for building a simultaneous PET/MRI system. This paper focuses on the performance assessment of the LabPET II DM in the presence of RF and gradient pulses and on the improvements required to optimize its EMI-compatibility. In the subsequent sections, the LabPET II electronics as well as the RF and gradient coil set-up are described, followed by an in-depth characterization and optimization of the MR-compatibility of the standard LabPET II DM and its shielded version.

## 2. Materials and methods

The electromagnetic interferences and compatibility (EMI/EMC) of LabPET II DMs were investigated outside an MRI scanner, using custom-designed RF transmitters and a small coil generating the magnetic field gradient. This experimental set-up provided maximum flexibility and allowed examining each component separately, with various shielding configurations, while assessing specific DM pixels, whenever needed. In addition, as the front-end electronics circuit of LabPET II requires some modifications to be fully MRI compatible in terms of size and material selection, this approach reduces the risk of damaging the MRI system.

First, the front-end electronics of the LabPET II modules, including the architecture of the dedicated mixed-signal ASIC, used to read out and process the PET signals, will be briefly described. Then, the custom-designed RF and gradient coils and the experimental set-up employed to carry out the measurements will be described. Finally, the choice of the shielding material and the methods applied to assess and suppress the EMI effects on the energy and timing resolution of the LabPET II DM will be explained.

### 2.1. LabPET II building blocks

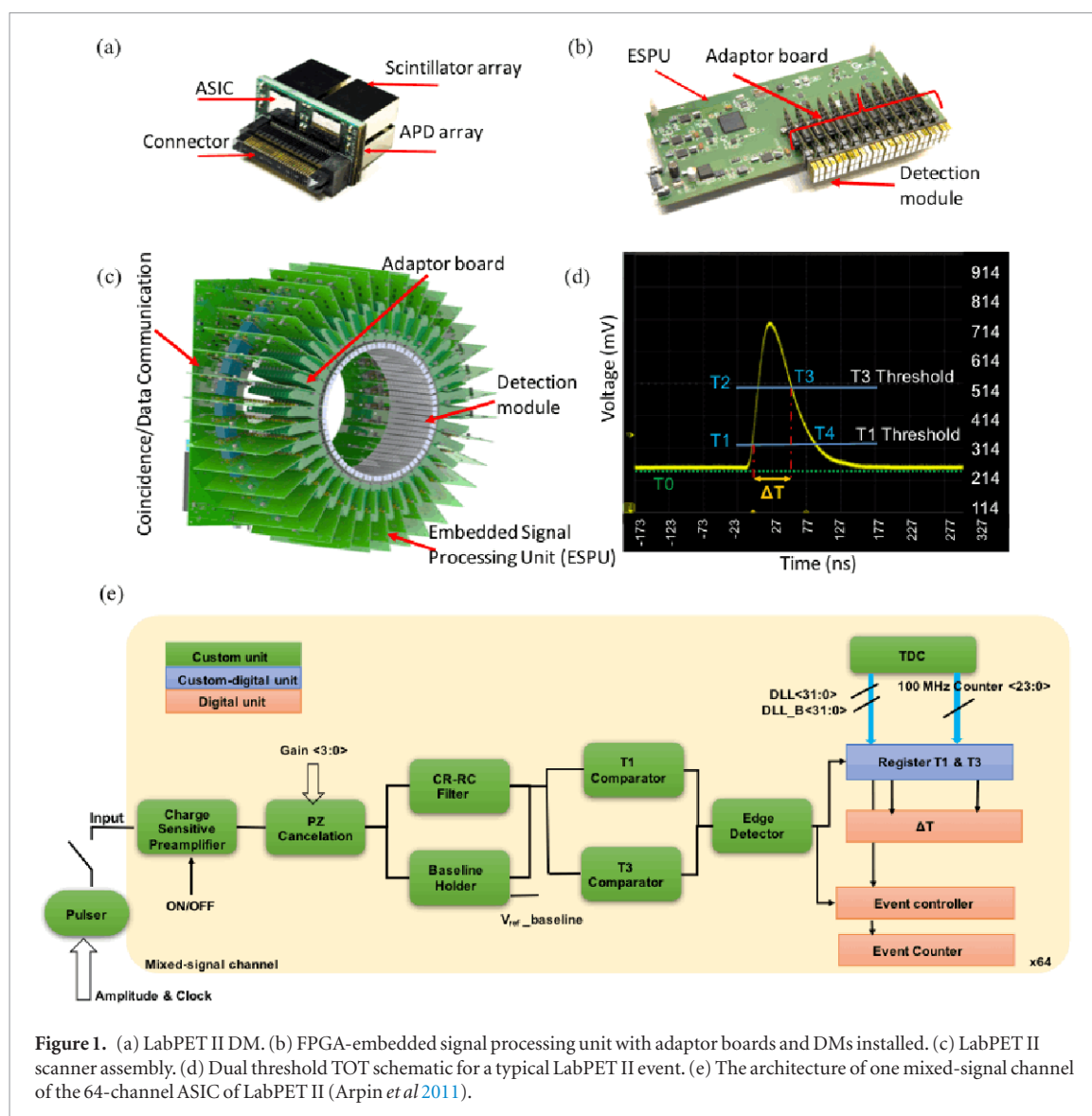
The LabPET II technology is a fully digital PET detection platform developed at Université de Sherbrooke to achieve submillimeter spatial resolution in small animal and millimeter resolution in larger structures such as the human brain. It is based on a true one-to-one coupling of crystals with APD pixels and independent parallel readout and processing of each pixel (Berard *et al* 2008, 2009, Bergeron *et al* 2015). The LabPET II DM (figure 1(a)) consists of four  $4 \times 8$  LYSO scintillator arrays mated with four  $4 \times 8$  APD arrays. The individual pixel size is  $1.12 \times 1.12 \times 12 \text{ mm}^3$  at a pitch of 1.2 mm. The signals from individual APD pixels are routed to the input channels of two 64-channel application-specific integrated circuits (ASICs) designed in a mixed-signal TSMC CMOS  $0.18 \mu\text{m}$  technology (Arpin *et al* 2011). For each detected event, the ASIC generates a 46-bit data event including the pixel address along with two timestamps at a 312.5 ps resolution. The first one derived from the rising edge of the signal indicates the time of interaction, and the second one, on the trailing edge, is used as an indicator of the deposited energy based on a time over threshold (TOT) scheme. The adaptor board (figure 1(b)) provides a regulated voltage supply to the individual APD arrays and supports the data transfer to an FPGA housed on the embedded signal processing unit (ESPU) board. The FPGA executes DM calibration, applies corrections for time propagation delays, sorts the data in chronological order and merges all events from the DMs mounted on the ESPU board (Njeimana *et al* 2012). The ESPUs are fanned into a coincidence, communication and gating unit (CCGU). The PET data transfer is performed through low-voltage differential signaling (LVDS) links. The entire scanner assembly is displayed in figure 1(c) showing the coincidence board, the adaptor boards, and the DMs. The scanner is connected to a remote PC through a 100 Mbits  $\text{s}^{-1}$  Ethernet link for configuration and through a 1 Gbit  $\text{s}^{-1}$  user datagram protocol (UDP) optical link for PET data transfer (Samson *et al* 2018).

Built-in temperature sensors in each ASIC of LabPET II, as well as those located on each ESPU, allow temperature monitoring at every location in the scanner. Furthermore, a quadrate fan cool down the LabPET II electronics. Nonetheless, the airflow was not sufficient for some of the studied conditions and a temperature variation was observed. In such cases, a heat pipe was installed at the back of the adaptor boards, while it was in contact with the ASIC using a thermally conductive layer of graphite sheet.

The analog signals are digitally converted in the ASIC in close proximity to the APD array; besides, the front-end electronic circuits have a limited bandwidth  $<20 \text{ MHz}$ ; hence, the possibility of introducing MRI noise in PET primary data is substantially reduced. Moreover, differential signaling, used to transfer both data and clock, in combination with a proper grounding scheme minimizes potential interferences of the gradient switching. In addition to the aforementioned noise attenuation measures, removing all ferromagnetic materials, such as the adaptor board connector, from the scanner FOV or using components in very small packaging sizes were also considered as the future work to minimize the inhomogeneity of the magnetic field. Considering that the LabPET II ASICs are made of silicon and aluminum, which are paramagnetic materials, and taking into account that the other components in modified LabPET II DM will be selected with a small footprint to accommodate the limited PCB size, from the material point of view, the modified LabPET II DM will be an MR-compatible unit that preserves the magnetic field homogeneity (Moghadam *et al* 2019). Further information on the LabPET II technology can be found in Bérard *et al* (2009), Arpin *et al* (2011), Njeimana *et al* (2012), Bergeron *et al* (2015) and Gaudin *et al* (2019).

### 2.2. LabPET II ASIC

The LabPET II ASIC enables the estimation of the energy and the time of interaction of detected radiation based on a dual-threshold time-over-threshold (dTOT) technique (Kipnis *et al* 1997, Akesson *et al* 2001, Powolny *et al* 2008). The dTOT schematic with two thresholds, applied to a typical LabPET II signal, as well as the architecture of one mixed-signal channel in the LabPET II ASIC are shown in figures 1(d) and (e), respectively. The signal from the APD (or from a pulser for testing purposes) at the input of a channel of the ASIC passes through a



charge sensitive pre-amplifier and a pole-zero cancellation unit, then it is amplified via a first-order CR-RC shaper (e.g. the curve of figure 1(d)). A baseline holder ensures a stable DC level at the shaper output to remove undesirable leakage current in the APD and efficiently register the timestamps. Two digital-to-analog converters set the desired thresholds of two comparators whose outputs trigger a 312.5 ps delay-lock loop-based time-to-digital converter and generate timestamps for the crossing voltage at  $T_1$  and  $T_3$ , where  $T_1$  is the leading edge crossing time of the first threshold and  $T_3$  is the falling edge crossing time of the second threshold, as shown in figure 1(d) (Arpin *et al* 2011). Event energy  $E$  is related non-linearly to the time-over-threshold data (Chang *et al* 2017) by an exponential monotonically increasing function of the form  $\Delta T = T_3 - T_1 = a + b \times \ln(E)$ , where  $a$  and  $b$  are constants to be fitted for each individual detector pixel. The two desired thresholds for optimal timing and energy measurements are set according to the optimized time jitter function over time as described in Njeimana *et al* (2012). Note that both energy and time-related stamps generated by the ASIC require correction factors applied in the ESPU to compensate for the time walk on  $T_1$  associated with the event energy. The event is registered as digital data in the ASIC and sent to the ESPU via a dedicated 100 Mbits  $s^{-1}$  LVDS serial link.

### 2.3. Energy and timing resolution measurement set up

Two LabPET II detection modules (DM #1 and DM #2), described in section 2.1, were placed face to face and approximately  $\sim 4$  cm apart. The TOT energy and timing measurements were conducted in the presence of RF coils transmitting signals with center frequencies equivalent to the Larmor frequencies of 3 T, 7 T, and 9.4 T MRI, respectively. Then the RF coil was replaced by the gradient coil and the measurements were repeated in the presence of a gradient coil switching from 10 kHz to 100 kHz. The data acquisitions were made with an 18.5 MBq  $^{68}\text{Ge}$  rod source positioned midway between the two DMs. The DMs were calibrated without turning on any coil and the same calibration was used for all measurements performed under the same conditions. If



the configuration was changed, e.g. inserting the shielding layer or temperature changes, then the calibration was redone before starting the new series of measurements. The experimental baseline voltages and equivalent noise values of the DMs were computed from the baseline histogram acquired for each pixel using a custom routine specifically developed for the LabPET II ASIC calibration. The routine consisted of sweeping the  $T1$  threshold while monitoring the channel count rate (Arpin *et al* 2011). The standard deviation of the noise count-rate distribution is equivalent to the noise presented at the charge sensitive amplifier input multiplied by the electronic gain. The baseline voltage and the RMS noise of the analog signal for all pixels were recorded before starting a 12 h acquisition for coincidence time resolution measurements. Meanwhile, the TOT energy spectra for each pixel of the APD arrays using a wide energy window from 250 keV to 1000 keV were stored. The same measurements were carried out for the DMs with RF pulses and gradient switching, independently.

## 2.4. Choice of shielding material

In order to eliminate EMIs, a shielding layer is required. To choose an appropriate shielding material, two factors must be essentially considered; (i) the shielding effectiveness (SE) and (ii) the induced eddy current. To shield the electromagnetic interferences, a layer of conductive paint from Parker Chomerics named CHO-SHIELD® 2056 was selected and its properties were compared with copper and carbon fiber. The composites by nature have higher electrical resistivity than metallic materials such as copper, with a resistivity of  $1.7 \times 10^{-8} \Omega \cdot \text{m}$ . As for CHO-SHIELD® 2056 paint, the surface resistance is  $3 \times 10^{-2} \Omega \text{ m}^{-2}$  based on its datasheet (Parker-Chomerics 2019). For a dry film with a thickness of 1 mm, the electrical resistivity was calculated as  $3 \times 10^{-5} \Omega \cdot \text{m}$ , which is a 3-order of magnitude higher than that of copper. This CHO-SHIELD® 2056 coating is a silver/copper filled conductive acrylic paint with a cost-effective and environmentally stable EMI shielding property.

### 2.4.1. Shielding effectiveness

The SE was measured using a modified version of the ASTM D4923-99 standard (Vasquez *et al* 2009) for the megahertz frequency range. In addition, a modified version of IEEE Std 299.1-2013 (Ishii and Yamazaki 2014) was used for determining RF attenuation at kilohertz frequency range; a similar method was also used for evaluating the RF attenuation of different optically transparent materials in PET/MRI applications (Parl *et al* 2017).

### 2.4.2. Eddy current measurement

Based on Faraday's Law, the magnitude of eddy currents depends on the alteration rate of the stimulating magnetic field. Consequently, fast imaging sequences, such as Echo-planar imaging sequences, in which gradients are quickly switched on and off, produce the largest and the most severe eddy current artifacts. Note that the eddy current effects due to RF signal variations are insignificant. A simple set-up was designed to measure eddy current induction for different materials, e.g. copper, carbon fiber and CHO-SHIELD® 2056. To assess the eddy currents, two custom-build cylindrical coils were made. The first coil was connected to an alternating current source at 100 kHz and located over the tested shielding layer. The thickness of copper and conductive paint samples was 1 mm; that is, five skin depths of copper at 100 kHz, whereas the thickness of carbon fiber was 3 mm, based on the data presented at Peng *et al* (2014). The second coil was used to monitor the phase and amplitude variations of the received signals. Note that, the 100 kHz gradient switching was selected for this specific test since it imposes the highest amount of interaction to the DM compared to the other frequencies of the gradient coil. The ratio between initial voltage and secondary induced voltage observed on an oscilloscope is a proper quantity to compare any eddy current induction since the induced current generates an opposite field decreasing the secondary voltage.

## 2.5. Mutual RF interferences between the LabPET II and the RF coil

To facilitate the measurements of RF coil interferences on the LabPET II performance, three small hexagonal coils were designed using copper tape and capacitors (one variable capacitor to adjust the frequency and five fixed capacitors) according to Larmor frequency (figure 2(a)). The RF coil is powered up with a signal generator connected to an RF amplifier [Empower, Model: 1112-BBM1C3KCK]. Since the gain of this amplifier is nonlinear, a higher power was applied to the 3 T coil than the 7 T or 9.4 T coils. Although the power of the RF coil, a maximum of 25 W, was lower than that of a real MRI scanner, it allowed achieving the key objectives, which included determining the electromagnetic interferences at specific frequencies as well as demonstrating viable approaches for eliminating those effects.

The clock frequency of LabPET II electronics was set at 100 MHz and the center frequencies of RF coils were set at 127.74 MHz, 298 MHz, and 400.25 MHz, corresponding to 3 T, 7 T, and 9.4 T MRI scanner, respectively. In the following sections, these frequencies are often replaced by their associated magnetic field. The three next subsections will describe the methodology to evaluate the RF coil response in the presence of LabPET II electronics, the RF signal effects on LabPET II performance and some approach to eliminate EMI effects of RF pulses on LabPET II DM.

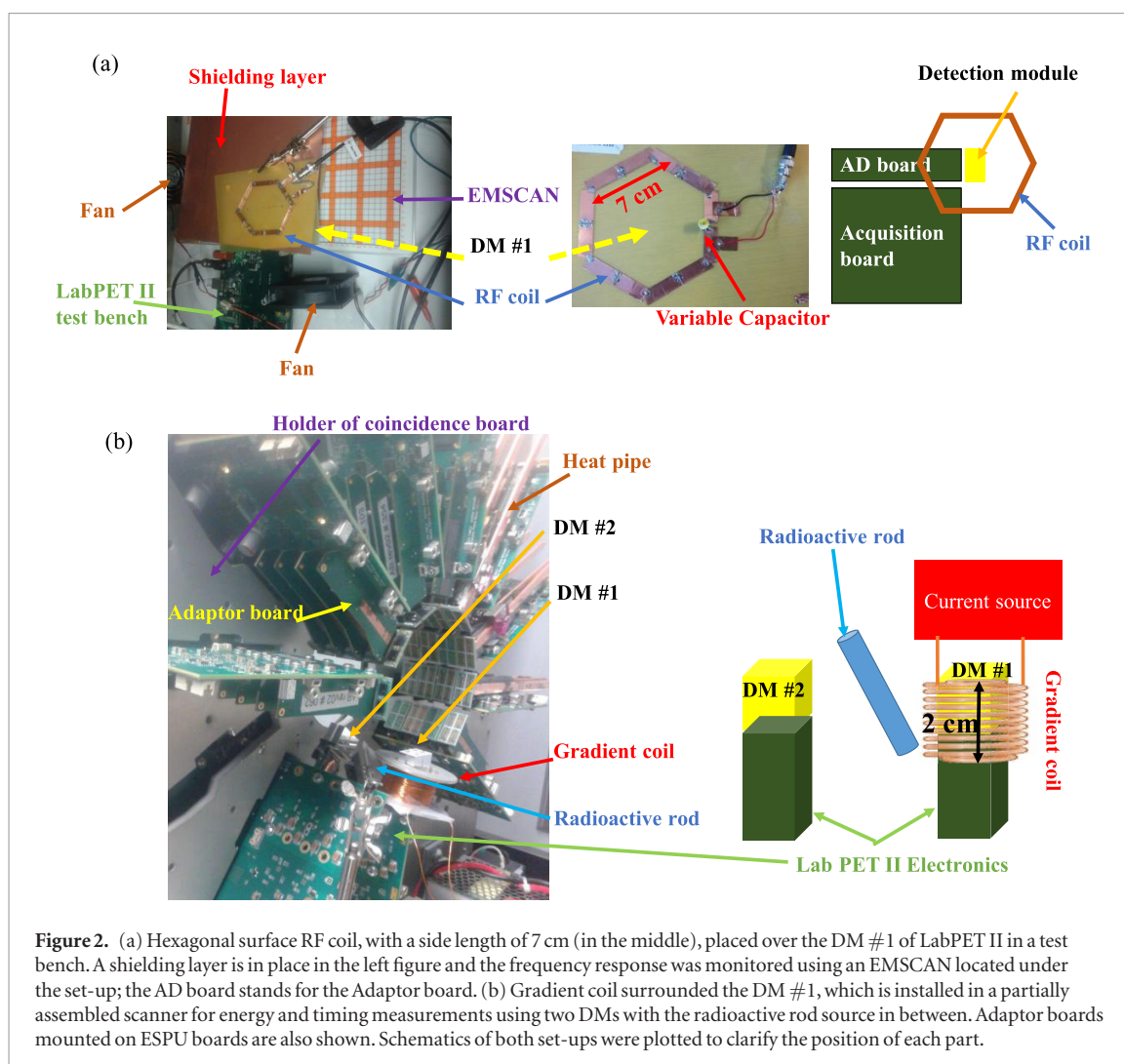


**Figure 2.** (a) Hexagonal surface RF coil, with a side length of 7 cm (in the middle), placed over the DM #1 of LabPET II in a test bench. A shielding layer is in place in the left figure and the frequency response was monitored using an EMSCAN located under the set-up; the AD board stands for the Adaptor board. (b) Gradient coil surrounded the DM #1, which is installed in a partially assembled scanner for energy and timing measurements using two DMs with the radioactive rod source in between. Adaptor boards mounted on EPU boards are also shown. Schematics of both set-ups were plotted to clarify the position of each part.

### 2.5.1. RF coil response in the presence of LabPET II electronics

The interaction between the RF coil signal and the LabPET II clock/signal was measured with an EMSCAN [EMxpert: EHX-82] signal integrity analysis device connected to a spectrum analyzer [Agilent Tech., Model: N9935A] as an RF receiver (shown in figure 2(a)). The EMSCAN was placed under the test bench of the LabPET II electronics when the 100 MHz clock was turned on, and the RF coil was powered up at the three aforementioned frequencies, one at the time. The frequency response of the RF emission was monitored with the EMSCAN to detect interactions between the LabPET II clock and the different RF coil signals to ensure the preservation of the MRI signal-to-noise ratio.

### 2.5.2. RF coil effects on LabPET II performance

The RF coil was located parallel to the vertical side of the LabPET II DM #1 at a distance of 1.1 mm to optimize the power transfer to the LabPET II electronics. The 1.1 mm distance was left as a gap that would be filled by a shielding layer, leaving only a small gap ( $1.1 \text{ mm} - 1.0254 \text{ mm} = 74.6 \mu\text{m}$ ) between the RF shield and the DM. The performance of the LabPET II DM was investigated as described in section 2.3 with and without turning on the RF coil at desired MRI frequencies. To obtain consistent experimental conditions, the RF coil was in place for all the tests and the first measurement, performed without powering up the RF coil, was used as a reference. The configuration of the DMs is shown in figure 2(b). For the RF coil measurements, the gradient coil shown in figure 2(b) was removed and the RF coil was placed vertically near DM #1. Here, the cooling system only included a quadrate fan with a total airflow of 300 cubic feet per minute (CFM).

### 2.5.3. Eliminating EMI effects of RF coil on the LabPET II DM

#### 2.5.3.1. Shielding

To shield the RF coil from LabPET II emission and vice versa, a 1-mil thick sheet of FR4 covered by 1 mm of CHO-SHIELD® 2056 conductive paint was placed between the LabPET II DMs and the RF coil. The FR4 surface was initially cleaned by acetone and IPA, which was followed by a deionized water rinsing and  $\text{N}_2$  flow drying.

Next, a uniform layer of conductive paint with 1 mm thickness was deposited over FR4. The edges of the samples were confined using 1 mm thick microscope slides. The conducting paint layer was then dried at low temperature on a 50 °C hot plate for 24 h to avoid the formation of bubbles. The uniformity of the shielding layer was verified to be  $\pm 5\%$  using ellipsometry. Besides, the shielding layer was connected to the nearest LabPET II ground. The baseline voltage, the noise level, the TOT energy resolution and the coincidence time resolution of the two DMs were recorded after inserting the shielding layer between the RF coil and the DMs.

#### 2.5.3.2. Changing the clock frequency

The LabPET II electronics clock frequency was also changed from 100 MHz to 106 MHz for two main purposes; (i) to observe the response of received signals from RF coil at receiver point and (ii) to verify if the RF interference from the clock and the Double Data Rate memory type 3 (DDR3) can be eliminated from the RF coil response, in order to preserve the SNR of the RF coils. The baseline voltage and the noise level of the LabPET II DMs were also recorded.

## 2.6. Mutual interferences between the LabPET II and the gradient coil

### 2.6.1. Gradient switching effects on the LabPET II performance

To simulate the effect of the gradient switching, an alternating current source providing a maximum current of  $3.5 A_{\text{rms}}$  was used along with a coil to generate a slew rate higher than 200 T/m/s at frequencies between 10 kHz to 100 kHz. The coil was made of 200 turns of 22-AWG wire wrapped around a 30 mm diameter by a 20 mm long cylinder. DM #1 was surrounded by this gradient coil as displayed in figure 2(b) while DM #2 was kept intact. To exclude temperature drifts due to the confinement of the DM by the gradient coil, the coil was located around DM #1 for all the measurements, including the reference measurement without gradient switching. Since a stable temperature is critical to eliminate the lattice heating and the APD gain variations, after initial measurements, a heat pipe was also attached to the electronic board using a high thermal conductive graphite sheet. Such a configuration was devised to eliminate the effects of temperature variations because of the inserting shielding layer that impeded the normal flow of fans.

The baseline voltage and its associated noise measurements of the LabPET II DMs were performed without and with the gradient switching at 10 kHz, 50 kHz and 100 kHz. The TOT energy resolution of each DM and the coincidence time resolution between the two DMs were measured.

### 2.6.2. Eliminating EMI effects of the gradient switching on the LabPET II DM

#### 2.6.2.1. Shielding

Besides the temperature stabilization to remove the heat effects caused by the gradient switching, its low-frequency emission requires a shielding layer to eliminate the EMI effects on the LabPET II DM. A CHO-SHIELD® 2056 conductive paint layer deposited over a 0.18 mm thick electrical tape (Temflex™, Model: PC695), prepared using the same method as that of the RF shielding layer and connected to the nearest ground of LabPET II electronics, was employed as a shielding layer using two different configurations; (i) shielded inside the gradient coil or (ii) covered around the LabPET II DM. The baseline voltage, the noise level, the TOT energy resolution and the time resolution were measured in the presence of the gradient switching. The heat pipe cooling configuration was utilized for all these series of measurements. All the measurements in the presence of the RF signals and gradient pulses have been repeated three times.

## 3. Results

### 3.1. Choice of shielding material

#### 3.1.1. Shielding effectiveness

SE comparison between all three materials is presented in table 1. Our measurement result using modified ASTM D4923-99 indicates shielding effectiveness of 85 dB at 100 MHz for CHO-SHIELD® 2056 coating that is in a good agreement with CHO-SHIELD® 2056 datasheet (Parker-Chomerics 2011) and more than 80 dB for frequencies around 300 MHz and 400 MHz. All three results of SE are in the range of the standard SE required for the PET/MRI shielding (Lamey *et al* 2010). In addition, this shielding layer provides a maximum SE of 65 dB for low frequencies down to 10 kHz, based on our measurement using a modified version of IEEE Std 299.1-2013. As for the carbon fiber sheet, a 3 mm thick layer covered with one layer of copper tape, with a thickness of 0.0762 mm, provides SE of 47 dB at 81 kHz; carbon fiber layer alone offers SE of 35 dB at low frequencies (Peng *et al* 2014). At high frequencies, however, a carbon fiber layer offers SE of up to 60 dB for a frequency range from 100 MHz to 400 MHz (Greco *et al* 2012).

**Table 1.** The shielding effectiveness of different materials at various frequencies, for 1 mm copper or CHO-SHIELD, 3 mm of carbon fiber without Cu foil. The carbon fiber SE values were presented based on the literature (Greco *et al* 2012, Peng *et al* 2014).

Frequency	10–100 kHz	127.74 MHz	298 MHz	400.25 MHz
SE of CHO-SHIELD (dB)	~65	85	83	86
SE of carbon fiber (dB)	35	>60	>60	>60
SE of copper (dB)	~105	>198	>274	>307

**Table 2.** Eddy current effects of copper, carbon fiber and CHO-SHIELD® 2056 paint.

Material	Copper	Carbon fiber	CHO-SHIELD® 2056	Air
Signal ratio	0.914 ± 0.022	0.971 ± 0.035	0.993 ± 0.031	1.0

### 3.1.2. Eddy current measurement

The ratio of the signal induced on the secondary coil to the initial signal of the primary coil is reported in table 2. The eddy current test confirms that the signal loss for copper was around 8.6%, while the reduction of the received signal by inserting the CHO-SHIELD® 2056 layer was about 0.7%. Therefore, the effect of induced eddy currents, originating from this composite layer, is 12 times lower than that of the copper layer.

Thus, considering its trivial eddy current effects and appropriate SE, CHO-SHIELD® 2056 paint was selected as a shielding layer for the LabPET II DM. Hence, from hereafter in this paper, CHO-SHIELD® 2056 paint was employed as the shielding layer.

## 3.2. Mutual RF interferences between the LabPET II and the RF coil

### 3.2.1. RF coil response in the presence of the LabPET II electronics

The frequency response of the RF coil in the presence of the LabPET II DM for different frequencies measured from the EMSCAN is displayed in figure 3.

Figure 3(a) shows a peak at 100 MHz coming from the LabPET II clock and another at 127.74 MHz representing the RF coil center frequency of the 3 T MRI. The EMSCAN RF response measurements show that the electromagnetic emission of the LabPET II 100 MHz clock has no effect on RF coil response working at 127.74 MHz.

The 298 MHz and 300 MHz peaks, displayed in figure 3(b), are coming from the RF coil center frequency of the 7 T MRI and the 3rd harmonic of the LabPET II clock, respectively. The clock will not affect the amplitude and FWHM of the 7 T RF signal unless the RF coil bandwidth exceeds 2 MHz, which is extremely wide for typical MRI protocols.

The first peak in figure 3(c) is originating from the fourth harmonics of LabPET II clock and the DDR3 memory running at 400 MHz. The second peak is the RF coil center frequency of the 9.4 T MRI oscillating at 400.25 MHz. The DDR3 memory, working at 800 Mbps, produces a strong signal at 400 MHz, close to the 400.25 MHz frequency of the 9.4 T MRI. This signal could cause RF signal distortion depending on the RF signal bandwidth. Therefore, using an effective shielding for 400 MHz frequencies or changing the LabPET II clock frequency, which also controls the DDR3 frequency, might be critical to preserve the MRI signal-to-noise ratio for the 9.4 T MRI.

### 3.2.2. RF coil effects on LabPET II performance

The mean value and the RMS noise level of the baseline voltage with and without RF coil pulses for the two LabPET II DMs are shown in figures 4(a) and (b), respectively. The results confirm that the RF signal insignificantly affects the mean value of the baseline voltage, whether the DM is next to (DM #1) or away from (DM #2) the RF coil.

The differences in the noise level result from the noise induced by the electromagnetic field as it was only observed in the nearest module to the RF coil, i.e. DM #1. In figure 4(b), there is an increased noise level for APD #2 on ASIC #1, DM #1, in the presence of RF signals, indicating that some detectors may be more sensitive to EMIs than others. This problem will be further highlighted in figure 7(b) for other APDs. Note that environmental conditions may change during a series of measurements, resulting in slightly different APD performance due to APD calibration that is no longer optimal. In fact, some extra variance may be added to the baseline voltage because the dTOT thresholds were set based on the initial calibration without RF interferences.

As a result, the baseline voltage distributions were degraded, as displayed in figures 5(a) and (b) for two typical pixels of DM #1 processed by ASIC #1 (pixel 37) and ASIC #2 (pixel 92). For a meaningful comparison, the baseline histogram of one typical pixel (pixel 137) of DM #2, not subject to RF interferences, is also shown in figure 5(c), confirming insignificant changes in the baseline distribution. As the figures show, the baseline histograms of individual pixels, with or without RF signal, have the same peak position because the dTOT thresholds were not changed, which is consistent with the constant mean values reported in figure 4(a). However, the noise



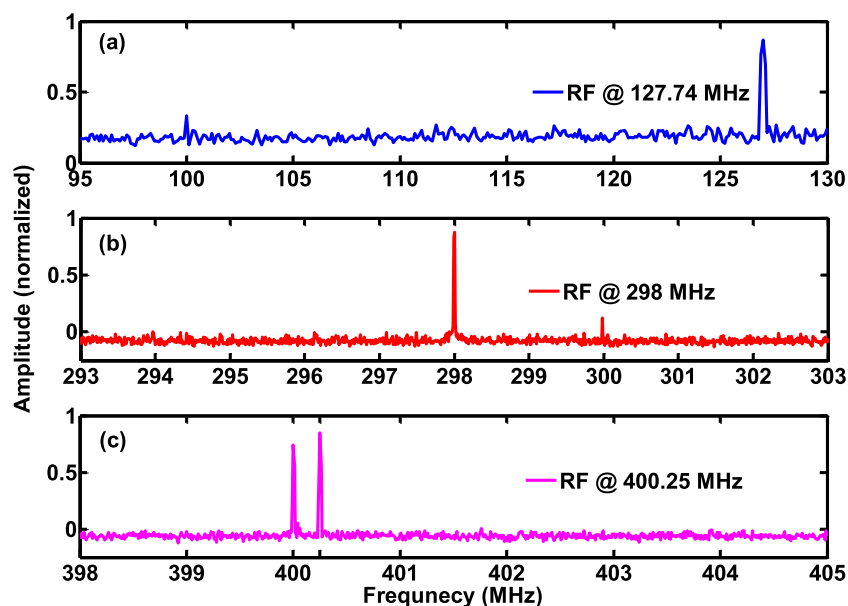


**Figure 3.** The normalized frequency response of signals received from LabPET II electronic and RF coil at frequencies of (a) 127.74 MHz (3 T), (b) 298 MHz (7 T), and (c) 400.25 MHz (9.4 T). The 100 MHz, 300 MHz, and 400 MHz peaks correspond to the clock signal, its 3rd and 4th harmonics.

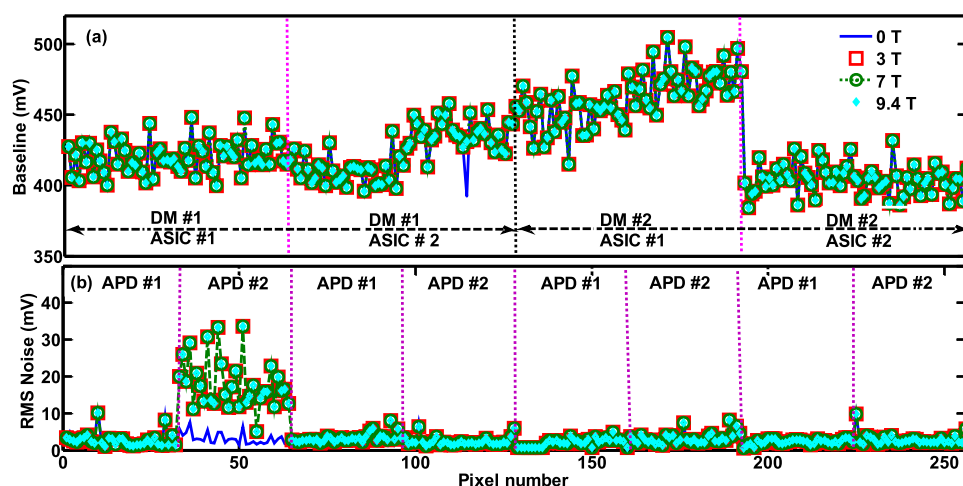


**Figure 4.** RF coil effects on LabPET II DMs: (a) baseline voltage and (b) RMS noise level without RF coil emission (0 T) and with RF emission at 127.74 MHz (3 T), 298 MHz (7 T) and 400.25 MHz (9.4 T). The pixels 1–128 belong to the DM #1 placed next to the RF coil and pixels 129–256 belong to the DM #2 located ~4 cm away from the RF coil. The same legend is used for both figures.

injected from the RF coil increases the standard deviation (or FWHM) of the baseline histograms for DM #1, as observed in figure 4(b).

Indeed the injected noise from the RF coil increases the number of times the baseline exceeds the lower noise threshold, thus the count rate in the baseline histograms. It also increases the standard deviation (or FWHM) of the baseline histograms for DM #1, as observed in figure 4(b). Note that the baseline histograms were acquired without any energy windows, consequently the histograms represent the low-energy electronic noise exceeding the lower noise threshold for a given pixel.

The energy spectra (in TOT) of one typical pixel of DM #1 of the LabPET II without and with RF signal for three frequencies of 127.74 MHz, 298 MHz, and 400.25 MHz are illustrated in figure 6(a). The results confirmed that the TOT signal amplitude decreases and the TOT energy resolution increases when the RF coil is turned on. Note that different pixels demonstrate different behavior; their photopeak position might shift to either left or right.

The average difference of the photopeak position from its initial value and the energy resolution of all pixels of ASIC#1, DM#1 for each condition are shown in table 3. The mentioned quantities for both APDs of ASIC#2, DM#1 are similar to the ASIC#1, APD#1.

The results demonstrate that the average position of energy photopeak in the presence of RF signals shifted to the left in comparison with the measurement without RF signal. The shift in the TOT energy spectrum can be

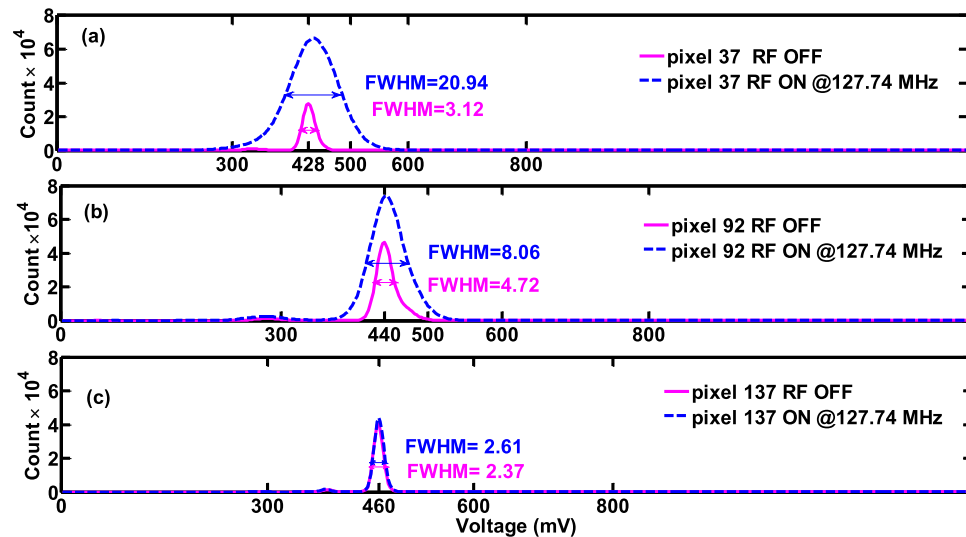


**Figure 5.** Histograms of the baseline for typical pixels from DM #1 exposed to the RF signal of a 3 T system: (a) pixel 37, (b) pixel 92; and for a typical pixel from DM #2 away from 3 T coil: (c) pixel 137 of APD #1 of ASIC #1.

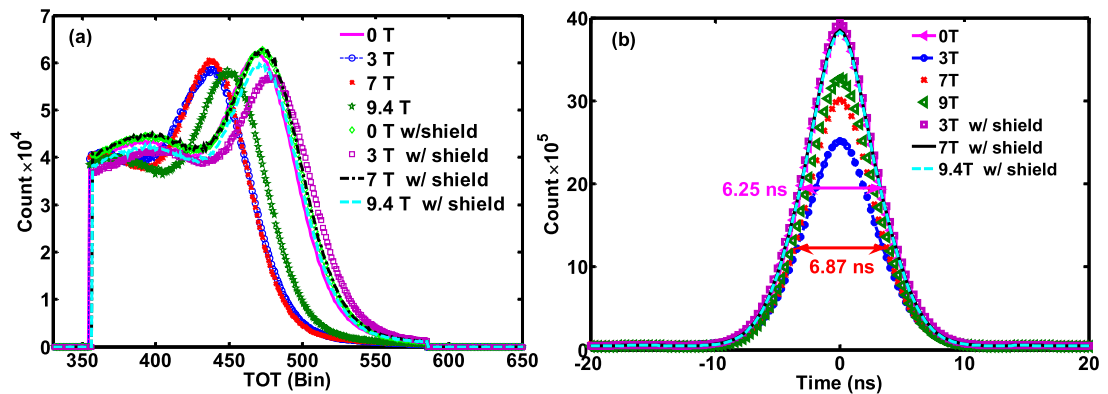


**Figure 6.** (a) The TOT energy spectra of one typical pixel without RF and with RF signal at the three characteristic frequencies of 127.74 MHz, 298 MHz and 400.25 MHz for 3 T, 7 T and 9.4 T. (b) Average coincidence time spectra of all coincident pixels between two LabPET II modules without and with RF signal at the three characteristic frequencies. The timing resolution for DMs without RF signal (0 T) and the worst case in the presence of the RF coil (7 T) were displayed in the figure, and all results are reported in table 4. The energy and time spectra after fixing with the shielding layer are also illustrated in the figures.

**Table 3.** Average difference of photopeak position from reference at 0 T and TOT energy resolution for all pixels of APD#1 and APD#2 of ASIC #1 of DM#1 with and without RF signals, with and without shielding. The negative sign means a lower bin.

	Position change ASIC#1, APD#1 (bin)	TOT resolution ASIC#1, APD#1 (%)	Position change ASIC#1, APD#2 (bin)	TOT resolution ASIC#1, APD#2 (%)
0 T	0	$9.9 \pm 3.2$	0	$9.6 \pm 1.8$
3 T	$-3 \pm 3$	$10.1 \pm 3.5$	$-23 \pm 11$	$13.6 \pm 6.2$
7 T	$-2 \pm 2$	$10.0 \pm 3.4$	$-20 \pm 5$	$10.7 \pm 2.6$
9.4 T	$-1 \pm 1$	$9.9 \pm 3.4$	$-12 \pm 3$	$10.0 \pm 1.5$
0 T w/shield	$0 \pm 1$	$9.9 \pm 3.1$	$0 \pm 1$	$9.6 \pm 1.7$
3 T w/shield	$-1 \pm 1$	$9.9 \pm 3.2$	$-2 \pm 1$	$9.7 \pm 1.8$
7 T w/shield	$-1 \pm 1$	$9.9 \pm 3.2$	$0 \pm 1$	$9.6 \pm 1.8$
9.4 T w/shield	$-1 \pm 1$	$9.9 \pm 3.1$	$-1 \pm 1$	$9.6 \pm 1.7$

explained by considering the calibration process and the noise level. In fact, the RF coil adds noise to the detector signal, which affects the  $T1$  and  $T3$  readings of the dTOT converter and provokes the shift of the TOT energy spectra. On the other hand, the degradation of the TOT energy resolution results from insufficient filtering of the high-frequency noise for pixel with elevated eddy current.

Coincidence time spectra between two LabPET II modules with DM #1 exposed to the RF coil under various conditions are plotted in figure 6(b) and the FWHM resolution for each condition is summarized in table 4. The

**Table 4.** Time resolution with and without RF signals for two DMs in coincidence, with and without shielding between the RF coil and DMs.

	FWHM (ns)
0 T	$6.25 \pm 0.10$
3 T	$6.43 \pm 0.31$
7 T	$6.87 \pm 0.30$
9.4 T	$6.72 \pm 0.30$
0 T w/shield	$6.25 \pm 0.10$
3 T w/shield	$6.31 \pm 0.12$
7 T w/shield	$6.30 \pm 0.11$
9.4 T w/shield	$6.26 \pm 0.11$

**Table 5.** The average count rate of DM #1 (128 pixels) with and without shielding in the presence of RF signals.

RF	No shield				Shielded			
	OFF	3 T	7 T	9.4 T	OFF	3 T	7 T	9.4 T
Count rate ( $\text{cps} \times 10^5$ )	$143 \pm 8$	$118 \pm 12$	$122 \pm 10$	$125 \pm 8$	$148 \pm 8$	$146 \pm 15$	$146 \pm 8$	$142 \pm 7$

results indicate  $6.25 \pm 0.10$  ns timing resolution for DMs without RF signal and an increase up to  $6.87 \pm 0.30$  ns in timing resolution in the presence of the RF signal. The time resolution results confirm that there is an impact on the timestamps generated by the dTOT technique that causes a deterioration of both timing and energy resolutions.

### 3.2.3. Eliminating EMI effects of the RF coil on the LabPET II DM

#### 3.2.3.1. Shielding

The energy spectra of a typical pixel and the coincidence time spectra of the shielded LabPET II DMs, shown in figures 6(a) and (b), confirm the efficiency of the conductive paint as a shielding material. The effects of each condition on the shielded LabPET II module were assessed quantitatively by data on photopeak position and energy resolution, as displayed in table 3. The values for 0 T were reported with and without shielding to have a reference for comparison. Note that for the shielded DM, there is an insignificant shift of photopeak to the left because of the statistical behavior of photon annihilation.

The coincidence time resolution (FWHM) data with shielding and RF signals are also summarized in table 4. The reference timing performance can be mostly restored with shielding. The integral of the energy spectra and coincidence time spectra were essentially the same for all the conditions, confirming that there would be no loss of counts despite the effects of RF interferences.

The results of the EMI effects originating RF signals on the LabPET II DM count rate are summarized in table 5, for shielded and not shielded DMs, as a mean of three measurements and its standard deviation. The count rate decreases in the presence of the RF signals while by shielding the DM the count rate was almost retrieved to its initial value.

The noise level of the baseline voltage when the DMs are exposed to RF emissions with and without shielding is displayed in figure 7(a). The condition without RF signals (0 T) is used as a reference. By inserting the shielding layer of conductive paint, the noise level is restored to the reference level.

#### 3.2.3.2. Changing clock frequency

Figure 7 also compares the RMS noise level of the LabPET II DMs, exposed to RF signals with 100 MHz and 106 MHz clock frequency (figure 7(b)). In both cases, the noise was picked up by several pixels, confirming the necessity to use appropriate shielding.

The frequency responses of the RF coil measured by the EMSCAN device, with the LabPET II clock triggering at 106 MHz, are shown in figures 8(a)–(c). The frequency responses, for all three MRI characteristic frequencies, show no distortion or interferences within the practical bandwidth of the RF coils, since there is no adjacent electronic signal emitting from the LabPET II electronics.

## 3.3. Mutual interferences between the LabPET II and the gradient coil

### 3.3.1. Gradient switching effects on the LabPET II performance

By placing a gradient coil around the DM #1, without heat pipe, and turning it on at 10 kHz, we observed an increase in the ASIC temperature readout from 48 °C to 62 °C, as there was no airflow to cool down the module. In comparison, the temperature of DM #2 was 45 °C. To avoid the temperature rise, heat pipes were added on the

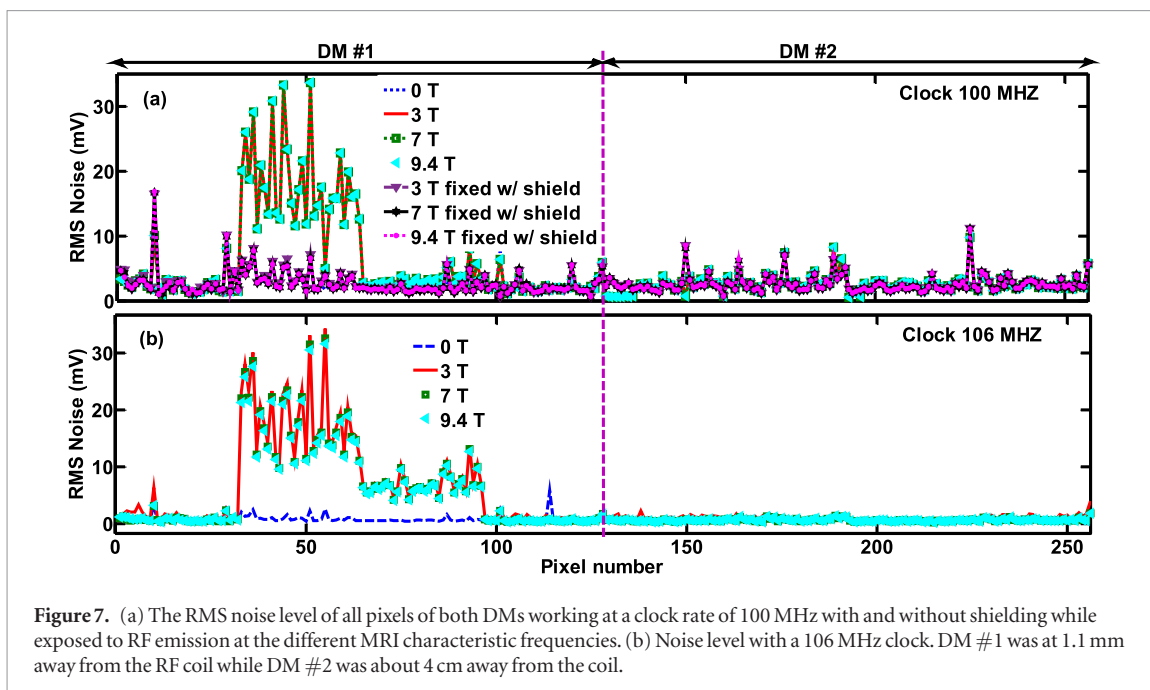


Figure 7. (a) The RMS noise level of all pixels of both DMs working at a clock rate of 100 MHz with and without shielding while exposed to RF emission at the different MRI characteristic frequencies. (b) Noise level with a 106 MHz clock. DM #1 was at 1.1 mm away from the RF coil while DM #2 was about 4 cm away from the coil.

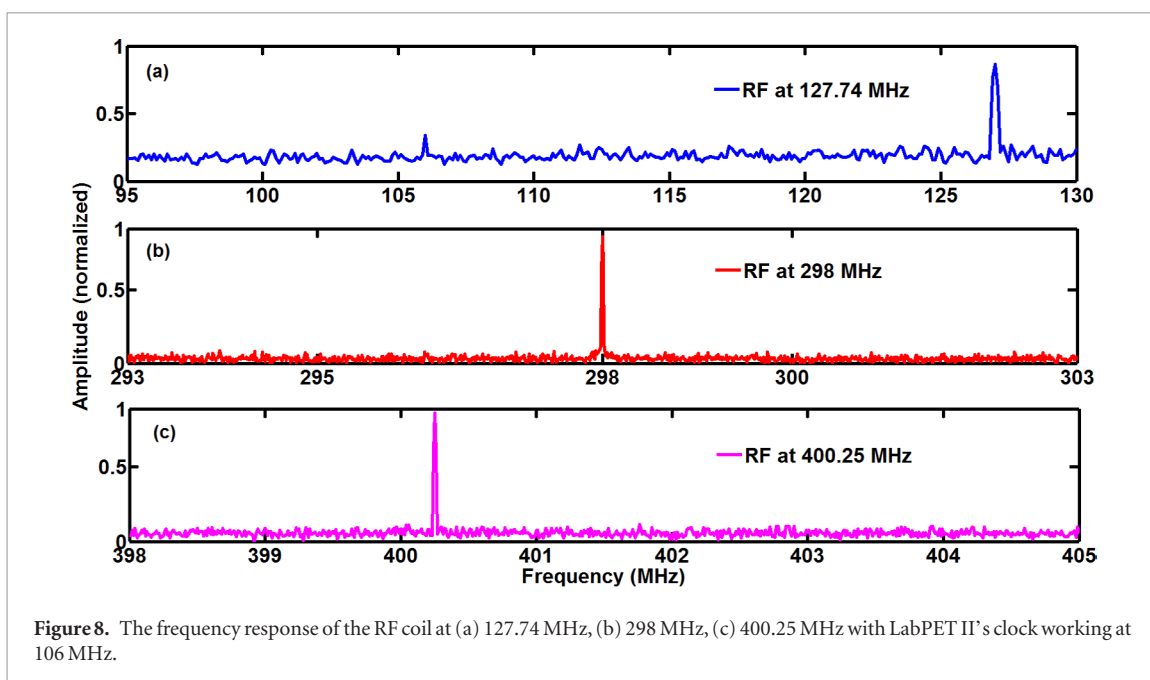
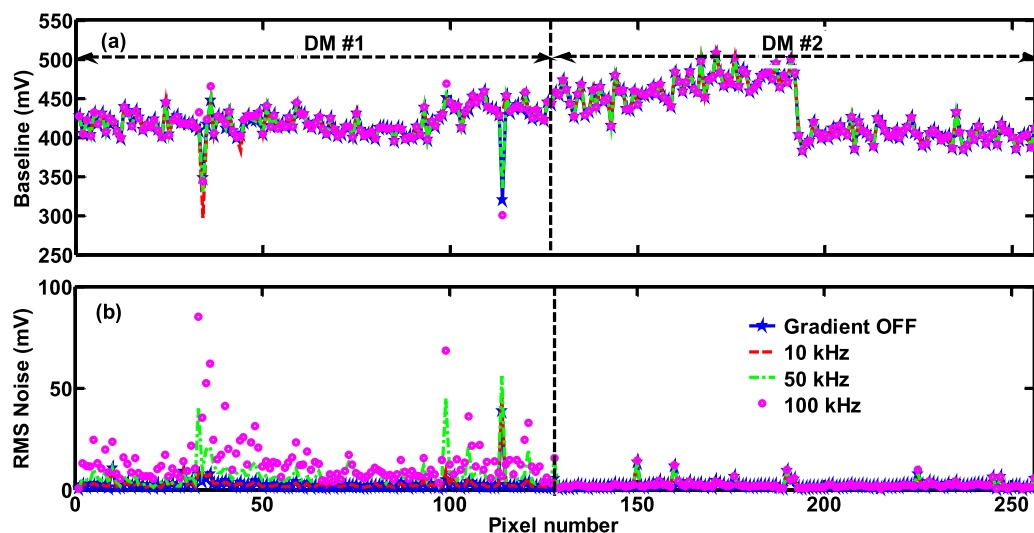


Figure 8. The frequency response of the RF coil at (a) 127.74 MHz, (b) 298 MHz, (c) 400.25 MHz with LabPET II's clock working at 106 MHz.

back of the adaptor board in contact with the ASICs of each DM. The average temperature of DM #1 and DM #2 then dropped to 41 °C and 39.5 °C, respectively. After stabilizing the temperature, the performance of DMs was reassessed, starting by recalibrating the set-up. The baseline voltage of each pixel with and without gradient switching are displayed in figure 9(a). The noise level of each pixel is also shown in figure 9(b). As the results demonstrate, the baseline voltage variations are insignificant for most pixels, however, the average RMS noise level of the DM #1 (pixels 1–128) is increased by turning on the gradient switching.

The energy spectra of one typical pixel of DM #1 with the gradient off and switching at 10 kHz, 50 kHz and 100 kHz are displayed in figure 10(a). The energy spectra demonstrate a downward shift of the photopeak position and a drop in the amplitude as the gradient switching frequency is increased. The TOT energy resolution of that pixel is degraded from 10% (for 10 kHz and no gradient switching) to 12.5% and 14.5%, at 50 kHz and 100 kHz switching frequencies, respectively. The degradation in energy resolution appears to be correlated with radio-frequency noise from gradient switching pulses. As a matter of fact, the gradient field is high enough to interfere with the LabPET II electronics and increase the noise at the T1 and T3 threshold crossings, which in turn degrades the accuracy of the TOT measurement. The TOT energy resolution of all the pixels for both DMs is shown in figure 10(b). An average 9.9% TOT energy resolution was observed for DM #1 without gradient switching and for DM #2 for all tests. The 10 kHz switching causes insignificant effects. However, gradient switching at 50 kHz or





**Figure 9.** (a) Baseline voltage and (b) RMS noise level of all pixels of the LabPET II DMs in the presence of the gradient coil without and with gradient switching at 10 kHz, 50 kHz and 100 kHz. DM #1 was inside the gradient coil and DM #2 was about 4 cm away from the coil. The same legend applies to both plots.

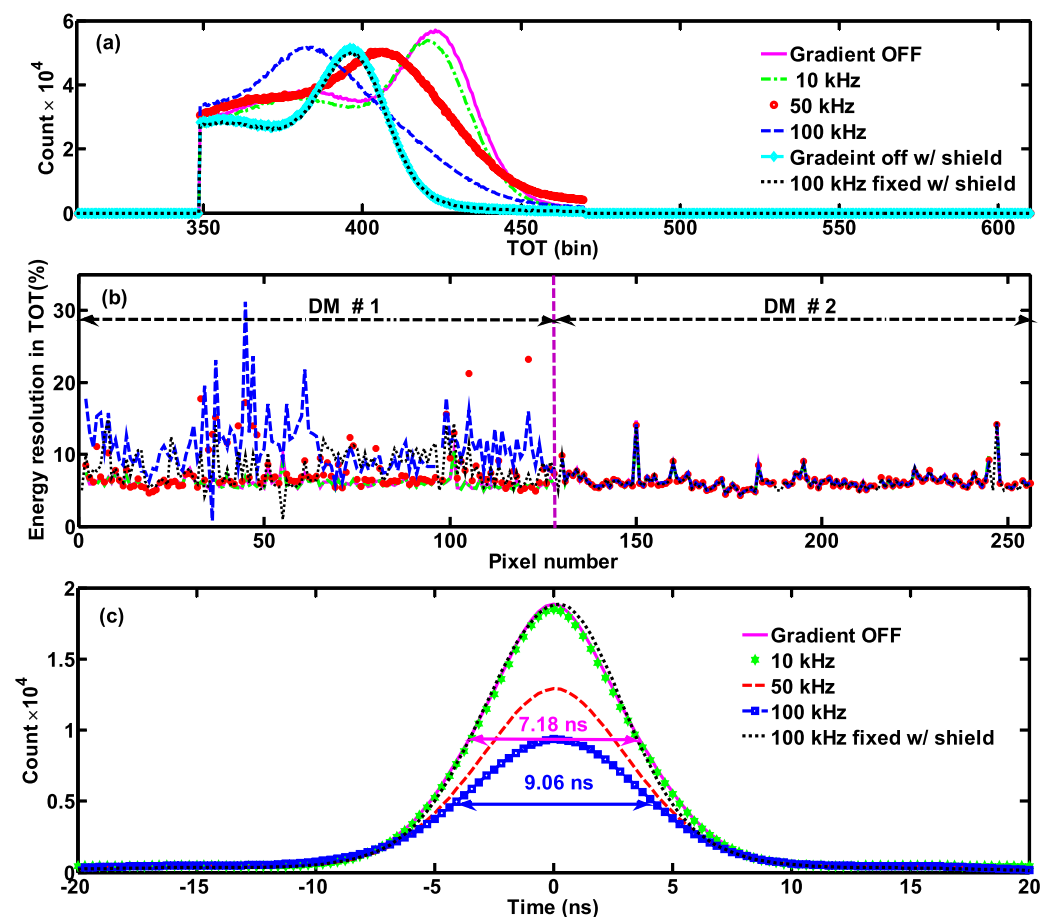


**Figure 10.** (a) The TOT energy spectra of a typical pixel of DM #1 without and with 10 kHz, 50 kHz and 100 kHz gradient switching; (b) the energy resolution for all the pixels in TOT bins without and with 10 kHz, 50 kHz and 100 kHz gradient; (c) coincidence time spectra of the two DMs without and with 10 kHz, 50 kHz and 100 kHz gradient switching. The results for shielded DM #1 from the 100 kHz switching are shown as a black dotted line. DM #1 was inside the gradient coil and DM #2 was about 4 cm away from the coil.

**Table 6.** The average count rate of DM #1 with and without shielding in the presence of the gradient switching signals.

Gradient	No shield				Shielded			
	OFF	10 kHz	50 kHz	100 kHz	OFF	10 kHz	50 kHz	100 kHz
Count rate (cps $\times 10^5$ )	120 $\pm$ 9	119 $\pm$ 10	115 $\pm$ 12	108 $\pm$ 16	98 $\pm$ 3	98 $\pm$ 5	98 $\pm$ 6	97 $\pm$ 4

100 kHz increases noise and deteriorates the average energy resolution to 12.9% at 50 kHz and 14.8% at 100 kHz. The difference in the average of the photopeak position and energy resolution of DM #1 and DM #2 are reported in supplementary tables S.1 and S.2 ([stacks.iop.org/PMB/65/035001/mmedia](https://stacks.iop.org/PMB/65/035001/mmedia)), respectively.

The coincidence time resolution between the two DMs is illustrated in figure 10(c). The gradient switching was first turned off (solid curve) and then turned on at 10 kHz (green stars), 50 kHz (red-dashed line) and 100 kHz (blue line with square), respectively. By increasing the frequency, the average FWHM time resolution increases slightly. In fact, with higher frequency, the magnetic field changes faster and induces more noise to the input of the DM, which distorted  $T_1$  recording. The quantitative data on the coincidence time resolution (FWHM) were summarized in supplementary table S.3.

Even though the temperature rise in the ASICs is stabilized by using a heat pipe, the interferences due to the EMI and eddy current effects on APDs and ASICs are still deteriorating the LabPET II performance.

### 3.3.2. Eliminating EMI on the LabPET II DM

#### 3.3.2.1. Shielding

The TOT energy spectrum for one typical pixel of shielded DM #1 as well as the TOT energy resolution of all pixels of shielded DM #1 and DM #2 for 100 kHz gradient switching are shown with dotted black lines in figures 10(a) and (b), respectively. These two curves indicate that the inserted shielding layer improved the energy resolution, as a result, the shielded DMs provided practically similar energy resolutions with and without gradient switching pulses. It is worth mentioning that inserting the shielding layer around the DM #1 caused increase in the temperature, which is observed as a shift of photopeak position to the left side for 0 T w/shield case in comparison with 0 T without shielding. The count rate with and without shielding layer in the presence of the gradient switching signals was displayed in table 6, demonstrating almost constant count rate value for different gradient switching frequencies for shielded DMs.

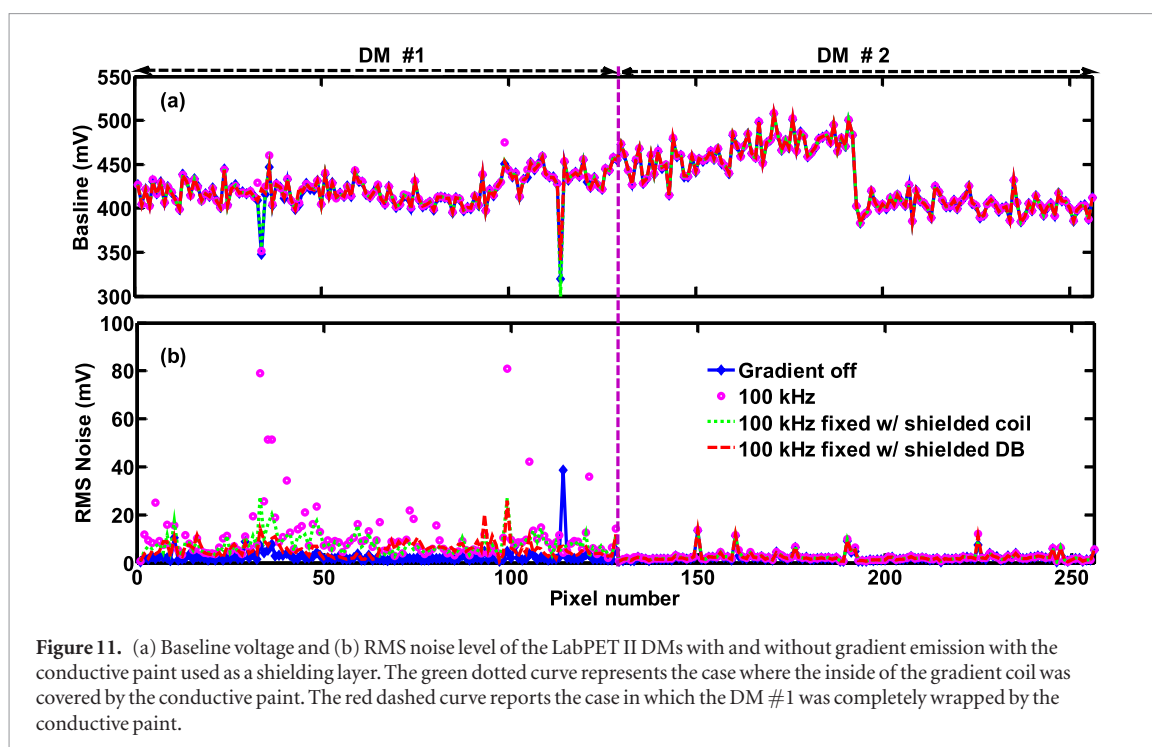
The timing resolution of two DMs in coincidence for the gradient switching at 100 kHz with shielding around the DM #1 is displayed in figure 10(c) with a dotted black line and the FWHM of each condition was also reported in supplementary table S.3. Results confirm that employing the shielding layer preserves the timing resolution of the LabPET II scanner. The timing resolution of  $7.18 \pm 0.10$  ns was obtained for shielded DM #1 with gradient switching, which is similar to that of the case without gradient. It is relevant to mention that the difference between timing resolutions for gradient test and RF coil test is due to the recalibration of voltages for each test.

The baseline voltage and noise level measurement with and without gradient switching at a constant temperature ( $\sim 4^\circ\text{C}$  more than the no-shielded DM) using the conductive paint shielding layer are shown in figures 11(a) and (b). The green dotted curve is associated with the test where inside the gradient coil was covered with the conductive paint and connected to the ground of the LabPET II coincidence board. This configuration decreases the noise by about 50%, which would be insufficient for the PET/MRI application. The dashed red curve displays the noise of the shielded DM #1. In this configuration, an insulator covered by the conductive paint was wrapped around the entire DM. This arrangement reduces the noise close to the initial noise value. However the temperature of the enclosed DM increases by  $4^\circ\text{C}$ . Therefore, it is plausible to consider that the previous configuration was unable to prevent gradient emission from reaching the APDs and ASIC inputs from ASICs and crystal sides, as the EMIs were not entirely compensated. The results endorse the fact that unwanted EMI effects, from low-frequency gradient switching, can be eliminated by this new shielding composite.

Similar coincidence time resolution is achieved with and without gradient switching using a proper shielding configuration. It confirms that the parameter related to the timing resolution ( $T_1$ ) obtained through the TOT technique was not affected for shielded DM. Consequently, variations in the noise level and energy resolution in these situations can be attributed to the temperature rise resulting from shielding confinement.

## 4. Discussion

The MR-compatibility of the LabPET II DMs through testing their performance in the presence of RF coils excited at frequencies corresponding to 3 T, 7 T, and 9.4 T magnetic field strength, as well as the switching gradient from 10 kHz to 100 kHz, was examined. The results demonstrate that the MRI coils cause insignificant interferences on the LabPET II DM when judiciously applying EMI shielding. Conversely, our measurements also indicate that



the RF response is immune to EM emission from the LabPET II module. A more comprehensive study inside real MRI scanners, however, should be carried out with a modified version of the LabPET II front-end electronics and the shielded coincidence board to further confirm these results.

The EMI measurement methods could be applicable to other ASIC based systems such as the PETsys TOF-PET 1&2 ASICs (Schug *et al* 2019), the Hamamatsu modules with their 18-channel ToT ASICs (Goertzen and Van Elburg 2019), or the Philips digital photon counter (DPC) based detectors (Brunner *et al* 2016). The same shielding method could also be used to enhance their EMI/EMC compatibility with an MRI scanner if needed. In addition, the same evaluation method could be applied to assess other shielding layers for their MR-compatibility in terms of eddy current induction.

In all measurements, it was important to determine whether the observed changes were due to genuine electromagnetic interferences or indirect side effects resulting from, for instance, temperature variations. Due to the confinement of the detector modules in the vicinity of the RF and gradient coils, there were temperature increases in many situations. For instance, the gradient coil completely surrounding the detector module induced a temperature increase of  $\sim 10^\circ\text{C}$ , on the other hand, the fast switching signal in the coil wires also generated  $I-R$  losses that increased the DM temperature of another  $\sim 4^\circ\text{C}$ . Increasing the APD temperature induces a drop of the APD multiplication gain that can be compensated by a bias correction of  $\sim 2\text{ V }^\circ\text{C}^{-1}$ , but it also increases the APDs leakage current and noise. The baseline holder embedded in the ASIC can sink up to  $3\text{ }\mu\text{A}$  of leakage current, while the individual APD leakage current is typically in the few nA range. Therefore, the effects of small temperature increment due to the DM confinement or RF and gradient interferences were easily compensated by the baseline holder and the baseline voltage level generally remained unchanged regardless of temperature variations. However, a  $\sim 15^\circ\text{C}$  increment in temperature could not always be compensated by the baseline holder. In fact, our first measurements without temperature stabilization showed some faulty pixels that could not be biased within the APD operating range. Considering typical APD characteristics, it may occur that increasing the temperature generates a dark current beyond the baseline holder limit saturating the front-end electronics and causing a preamplifier failure. Besides, if several pixels show high dark current, then the high voltage (HV) controller embedded in the ASIC is unable to provide the appropriate bias voltage due to the high total leakage current drained by the multiple acquisition channels of a detection array. In the case where the shielding and the heat pipe were present, as the heat was transferred efficiently, the dark current did not exceed the limit of the baseline holder and the temperature effects were not tangible.

The shift of energy spectrum, induced by the RF coil signals, was originally attributed to the frequency interferences and the temperature increments. Nevertheless, our studies confirmed that this effect is highly related to the electromagnetic interferences of the RF coil with LabPET II electronics. Although the built-in shaper filter in the ASIC was designed to attenuate frequency up to 20 MHz, the noise injection was observed in the LabPET II electronics due to the inability of filters to block the high-frequency noise for pixels with elevated leakage current. Consequently, by placing an RF coil close to the DM, the noise injected from the RF coil interacted with the ASIC

signals and changed the amplitude and the shape of the input signals. Accordingly, the initial calibration was no longer valid for some of the arrays and it caused a shift in the energy spectrum of each pixel of that specific array.

For gradient switching tests, as the temperature was stabilized by means of a heat pipe, the shifts of photoppeak position in the TOT energy spectra were induced by the gradient pulses and were not related to temperature variations. Hence, the EMIs had to be compensated by a shielding layer.

Considering the clock harmonics and DDR3 peak signal at 400 MHz, near the RF signal of 9.4 T MRI, the LabPET II electronic clock can be changed from 100 MHz to 106 MHz without detrimental effects, in order to eliminate any possible interferences of LabPET II signal with RF signal and preserve its SNR for different magnetic fields.

Based on the obtained results, an appropriate shielding configuration makes it possible to fabricate an MR-compatible PET scanner based on LabPET II DMs. In addition, by changing the shielding material from a metallic one to a conductive paint layer, the gradient EMIs were eliminated along with the possibility to decrease the gradient-induced eddy current effects. Nonetheless, the conductive paint layer showed excellent performance for shielding the low-frequency EMI and reducing the eddy currents. The proposed conductive paint has similar conductivity values as carbon fiber shielding for high frequencies (Peng *et al* 2014) while offering more flexibility, to cover the required surface, and lighter weight. Besides, this composite has shielding effectiveness of 65 dB for low frequencies down to 10 kHz to reduce unwanted low frequency switching interactions from gradients, whereas it is impossible to eliminate the interferences from gradient with carbon fiber. Thus, PET/MRI scanner based on carbon fiber shielding necessitates an additional layer of copper to eliminate the gradient effects, which in turn cause eddy current induction and chemical shift errors (Peng *et al* 2014). By applying a 1 mm layer of the conductive paint for shielding both RF and gradient switching EMI, the LabPET II DM experiences less eddy current induction and, consequently, it provides the possibility to acquire images with fast gradient switching sequences. Considering these criteria, shielded LabPET II DMs would appear as suitable candidates for an MR-compatible PET-insert with simultaneous PET/MRI imaging capability.

In this report, we focused on identifying possible interferences from RF coil and gradient switching of an MRI scanner and provided an approach to reduce the effects of those undesirable interactions for developing a simultaneous PET/MRI scanner based on the LabPET II DM. In future work, a ring of the shielded and modified LabPET II modules will be inserted in a clinical 3 T MRI to examine the effects of the PET-insert on MRI performance and to investigate the required techniques for eliminating any disturbing issues to design a true simultaneous PET/MRI for the human brain.

## 5. Conclusion

The results confirm the feasibility of using shielded LabPET II DMs in the presence of EMIs at the Larmor frequency of different MRI scanners. After some material modifications to remove ferromagnetic components, it would be a viable candidate for designing a simultaneous PET/MRI scanner with a submillimeter spatial resolution of PET images. By using the CHO-SHIELD<sup>®</sup> 2056 paint as an EMI shielding layer, not only the effects of frequency interferences from both the RF coil and gradient switching were compensated, but the eddy currents were also reduced owing to the lower conductivity of the shielding material. Furthermore, by stabilizing the temperature using heat pipes, the undesirable effects of APD gain variations due to temperature changes were eliminated. One key advantage of the LabPET II technology is that analog signals are digitized directly in the ASICs, very close to the APDs, making them much less prone to interferences. Further work will be conducted to verify the performance of a modified version of the LabPET II DM inside an MRI to confirm our findings.

## Acknowledgments

The authors would like to thank Christian Thibaudeau, Haithem Bouziri and Caroline Paulin for their help. This work was supported by *Le Fonds de Recherche du Québec—Nature et Technologies* (FRQNT) and the Natural Sciences and Engineering Research Council of Canada (NSERC). The authors would also like to acknowledge financial aid from the Quebec Bio-Imaging Network (QBIN) and to thank Matrix Technology Ltd for supplying the CHO-SHIELD<sup>®</sup> 2056 sample.

## ORCID iDs

Narjes Moghadam  <https://orcid.org/0000-0001-9101-4210>

Roger Lecomte  <https://orcid.org/0000-0002-8541-0783>



## References

- Akesson T et al 2001 Particle identification using the time-over-threshold method in the ATLAS transition radiation tracker *Nucl. Instrum. Methods Phys. Res. A* **474** 172–87
- Arpin L et al 2011 Embedded real time digital signal processing unit for a 64-channel PET detector module 2011 *IEEE Nuclear Science Symp. Conf. Record (Valencia, Spain, 23–29 October 2011)* pp 1545–50
- Bérard P et al 2009 Development of a 64-channel APD detector module with individual pixel readout for submillimetre spatial resolution in PET *Nucl. Instrum. Methods Phys. Res. A* **610** 20–3
- Berard P et al 2008 LabPET II, a novel 64-channel APD-based PET detector module with individual pixel readout achieving submillimetric spatial resolution 2008 *IEEE Nuclear Science Symp. Conf. Record (Dresden, Germany, 19–25 October 2008)* pp 5457–62
- Bergeron M et al 2015 LabPET II, an APD-based detector module with PET and counting CT imaging capabilities *IEEE Trans. Nucl. Sci.* **62** 756–65
- Beyer T et al 2000 A combined PET/CT scanner for clinical oncology *J. Nucl. Med.* **41** 1369–79 (PMID:10945530)
- Brunner S E et al 2016 A comprehensive characterization of the time resolution of the philips digital photon counter *J. Instrum.* **11** P11004
- Catana C et al 2006 Simultaneous acquisition of multislice PET and MR images: initial results with a MR-compatible PET scanner *J. Nucl. Med.* **47** 1968–76 (PMID:17138739)
- Chang C-M, Cates J W and Levin C S 2017 Time-over-threshold for pulse shape discrimination in a time-of-flight phoswich PET detector *Phys. Med. Biol.* **62** 258–71
- Cherry S R et al 2018 Total-body PET: maximizing sensitivity to create new opportunities for clinical research and patient care *J. Nucl. Med.* **59** 3–12
- Delso G and Ziegler S 2014 *PET/MRI: Methodology and Clinical Applications* ed L Carrio and P Ros (Berlin: Springer)
- Düppenbecker P M et al 2012 Gradient transparent RF housing for simultaneous PET/MRI using carbon fiber composites 2012 *IEEE Nuclear Science Symp. and Medical Imaging Conf. Record (NSS/MIC) (Anaheim, CA, 27 October 2012–3 November 2012)* pp 3478–80
- Düppenbecker P M et al 2016 Development of an MRI-compatible digital SiPM detector stack for simultaneous PET/MRI *Biomed. Phys. Eng. Express* **2** 015010
- Fox R T, Wani V, Howard K E, Bogle A and Kempel L 2008 Conductive polymer composite materials and their utility in electromagnetic shielding applications *J. Appl. Polym. Sci.* **107** 2558–66
- Gaudin E et al 2019 Performance simulation of an ultrahigh resolution brain PET scanner using 1.2 mm pixel detectors *IEEE Trans. Radiat. Plasma Med. Sci.* **3** 334–42
- Gebhardt P, Weissler B and Wehner J 2014 RESCUE—reduction of MR-SNR-degradation by using an MR-synchronous lowinterfering PET acquisition technique *EJNMMI Phys.* **1** A87
- Goertzen A L and Van Elburg D 2019 Performance characterization of MPPC modules for TOF-PET applications *IEEE Trans. Radiat. Plasma Med. Sci.* **3** 475–82
- Grazioso R et al 2006 APD-based PET detector for simultaneous PET/MR imaging *Nucl. Instrum. Methods Phys. Res. A* **569** 301–5
- Greco S, Tamburrano A, D' Aloia A, Mufatti R and Sarto M S 2012 Shielding effectiveness properties of carbon-fiber reinforced composite for HIRF applications *Int. Symp. on Electromagnetic Compatibility—EMC EUROPE (17–21 September 2012)* pp 1–6
- Ishii M and Yamazaki Y 2014 A study on measurement method of shielding effectiveness using loop antenna in low-frequency 2014 *Int. Symp. on Electromagnetic Compatibility (Tokyo, 12–16 May 2014)* pp 749–52
- Kang H G et al 2015 Assessment of MR-compatibility of SiPM PET insert using short optical fiber bundles for small animal research *J. Instrum.* **10** P12008
- Kang J et al 2009 Characterization of cross-compatibility of small animal insertable PET and MRI 2009 *IEEE Nuclear Science Symp. Conf. Record (NSS/MIC) (Orlando, FL, 24 October–1 November 2009)* pp 3816–21
- Kinahan P E, Townsend D W, Beyer T and Sashin D 1998 Attenuation correction for a combined 3D PET/CT scanner *Med. Phys.* **25** 2046–53
- Kipnis I et al 1997 A time-over-threshold machine: the readout integrated circuit for the BABAR silicon vertex tracker *IEEE Trans. Nucl. Sci.* **44** 289–97
- Ko G B et al 2016 Simultaneous multiparametric PET/MRI with silicon photomultiplier PET and ultra-high-field MRI for small-animal imaging *J. Nucl. Med.* **57** 1309–15
- Lamey M et al 2010 Radio frequency shielding for a linac-MRI system *Phys. Med. Biol.* **55** 995
- Levin D N, Pelizzari C A, Chen G T, Chen C T and Cooper M D 1988 Retrospective geometric correlation of MR, CT, and PET images *Radiology* **169** 817–23
- Moghadam N, Espagnet R, Bouchard J, Lecomte R and Fontaine R 2019 Studying the effects of metallic components of PET-insert on PET and MRI performance due to gradient switching *Phys. Med. Biol.* **64** 075003
- Njejjimana L et al 2012 Design of a real-time FPGA-based DAQ architecture for the LabPET II, an APD-based scanner dedicated to small animal PET imaging 2012 *18th IEEE-NPSS Real Time Conf. (Berkeley, CA, 9–15 June 2012)* pp 1–5
- Olcott P et al 2015 Prototype positron emission tomography insert with electro-optical signal transmission for simultaneous operation with MRI *Phys. Med. Biol.* **60** 3459–78
- Omidvari N et al 2018 MR-compatibility assessment of MADPET 4: a study of interferences between an SiPM-based PET insert and a 7 T MRI system *Phys. Med. Biol.* **63** 095002
- Parker-Chomerics 2011 Silver/copper-filled acrylic coating for EMI shielding CHO-SHIELD® 2056 (<https://www.parker.com/Literature/Chomerics/Parker%20Chomerics%20CHO-SHIELD-2056.pdf>)
- Parker-Chomerics 2019 *Technical Specification* (Online) <http://ph.parker.com/ca/en/cho-shield-2056-series-corrosion-resistant-conductive-coatings> (Accessed)
- Parl C et al 2017 A novel optically transparent RF shielding for fully integrated PET/MRI systems *Phys. Med. Biol.* **62** 7357–78
- Peng B J, Wu Y, Cherry S R and Walton J H 2014 New shielding configurations for a simultaneous PET/MRI scanner at 7 T *J. Magn. Reson.* **239** 50–6
- Pichler B, Kolb A, Nägele T and Schlemmer H 2010 PET/MRI: paving the way for the next generation of clinical multimodality imaging applications *J. Nucl. Med.* **51** 333–6
- Pichler B et al 1997 Performance test of a LSO-APD PET module in a 9.4 Tesla magnet 1997 *IEEE Nuclear Science Symp. Conf. Record (Albuquerque, NM, 9–15 November 1997)* vol 2, pp 1237–9
- Pichler B J, Wehrl H F, Kolb A and Judenhofer M S 2008 Positron emission tomography/magnetic resonance imaging: the next generation of multimodality imaging? *Semin. Nucl. Med.* **38** 199–208
- Powolny F et al 2008 A novel time-based readout scheme for a combined PET-CT detector using APDs *IEEE Trans. Nucl. Sci.* **55** 2465–74

- Samson A *et al* 2018 A fully automated and scalable timing probe-based method for time alignment of the LabPET II scanners *Nucl. Instrum. Methods Phys. Res. A* **889** 1–6
- Saoudi A and Lecomte R 1999 A novel APD-based detector module for multi-modality PET/SPECT/CT scanners *IEEE Trans. Nucl. Sci.* **46** 479–84
- Schenck J F 1996 The role of magnetic susceptibility in magnetic resonance imaging: MRI magnetic compatibility of the first and second kinds *Med. Phys.* **23** 815–50
- Schug D, Nadig V, Weissler B, Gebhardt P and Schulz V 2019 Initial measurements with the PETsys TOFPET2 ASIC evaluation kit and a characterization of the ASIC TDC *IEEE Trans. Radiat. Plasma Med. Sci.* **3** 444–53
- Schug D *et al* 2016 Initial PET performance evaluation of a preclinical insert for PET/MRI with digital SiPM technology *Phys. Med. Biol.* **61** 2851–78
- Schulz V *et al* 2009 A preclinical PET/MR insert for a human 3T MR scanner 2009 *IEEE Nuclear Science Symp. Conf. Record (NSS/MIC)* (Orlando, FL, 24 October 2009–1 November 2009) pp 2577–9
- Seydou Traore M *et al* 2015 System architecture of a fully combined PET/CT scanner using LabPET™ electronics with an upgraded analog front-end optimized for PET and CT counting mode operation 2015 *IEEE Nuclear Science Symp. and Medical Imaging Conf. (NSS/MIC)* (San Diego, CA) (<https://doi.org/10.1109/NSSMIC.2015.7581980>)
- Slomka P J 2004 Software approach to merging molecular with anatomic information *J. Nucl. Med.* **45** 36S–45S (PMID:14736834)
- Soret M, Bacharach S L and Buvat I 2007 Partial-volume effect in PET tumor imaging *J. Nucl. Med.* **48** 932–45
- Spanoudaki V C, McElroy D P, Torres-Espallardo I and Ziegler S I 2008 Effect of temperature on the performance of proportional APD-based modules for gamma ray detection in positron emission tomography *IEEE Trans. Nucl. Sci.* **55** 469–80
- Townsend D W 2008 Multimodality imaging of structure and function *Phys. Med. Biol.* **53** R1–39
- Vasquez H, Espinoza L, Lozano K, Foltz H and Yang S 2009 Simple device for electromagnetic interference shielding effectiveness measurement *IEEE EMC Soc. Newsletter* **220** 62–8